# Polarization of MeerKAT Calibrators

Russ Taylor
Inter-University Institute for Data Intensive Astronomy

Sam Legodi
South African Radio Astronomy Observatory

15 March 2021

**Summary**

We report on full-Stokes L-band observations of 98 MeerKAT calibration sources. Linear polarization is detected in 69 objects above a fractional level of 0.2%. We identify ten sources with strong fractional linear polarization and low Faraday Rotation Measure that could be suitable for wide-band absolute polarization calibration. A monitoring program would allow us to assess if their polarization properties are stable with time.

We detect significant circular polarization from 18% of the sample down to a detection level of 0.1%. Circularly polarized emission is seen only for flat spectrum sources $\alpha > -0.5$.

We compare our polarized intensities and Faraday Synthesis results to data from the NVSS at 1400 MHz and the ATCA SPASS survey at 2300 MHz. NVSS data exists for 54 of our sources and SPASS data for 20 sources. The the percent polarization and Rotation Measures from both surveys agree well with our results.

The residual instrumental linear polarization for these observations is measured at 0.16% and the residual instrumental circular polarization is measured at 0.06%. These levels may reflect either instabilities in the relative bandpass between the two polarization channels with either time or antenna orientation, or atmospheric/ionospheric variations with pointing direction. Tracking of the hourly gain solutions on J0408-6545 after transfer of the primary gain solutions suggest an deterioration of the gain stability by a factor of several starting about two hours after sunrise. This suggests that observing during the night time could dramatically improve the precision of polarization calibration.

# Contents



# 1 Introduction

For telescopes with linear polarized feeds, polarized signals target radio sources are mixed into all correlation products. It is therefore important for both observational planning and precise calibration to have knowledge of the polarization of calibration sources. To this end, we have observed 98 MeerKAT gain calibration sources at L-band in full polarization to measure their polarization properties.

# 2 Observations

The calibration sources were observing during one of two observing runs carried out by the SARAO commissioning team. The first run on 19 August 2019 and the second run on 29 August 2020. The first run observed 52 sources in the RA range 11–23 hours, and second run observed 46 sources in the RA range 00-11 hours. Both observing runs were about 12 hours long. Each target source was observed for a short scan of about 5 minutes. The strong unpolarized source J1939-6342 was observed several times during the each run, and the absolute polarization calibrator J1331+3030 (3C286) was observed twice for 5 minutes at the beginning of the first run, and once for 10 minutes at the end of the second run.

# 3 Calibration and Imaging

The data were processed on the Ilifu cloud using a customized version of the IDIA calibration and imaging pipeline[1]. The pipeline partitions the L-band RF MHz into 15 spectral windows between 880 MHz to 1680 MHz. Data in frequency ranges with strong

[1]`https://idia-pipelines.github.io/docs/processMeerKAT`

persistent RFI (933–960MHz, 1163–1299 MHz, and 1525–1630 MHz) are removed at this partition stage. Each spectral window is split into its own multi-MS that is processed concurrently using the SLURM job manager. Following calibration the calibrated data from each spectral window is merged into a single measurement set with calibrated visibilities.

For ideal linear feeds (except for leakage), the linear approximation to the response of the parallel and cross hand visibilities is given the equations 1-4 below. In these equations we have retained only those leakage terms that multiply Stokes $I$. A more complete set including leakage terms that multiply the source polarization can be found in [4].

$$V_{xx} = g_x^i g_x^k (I + Q\cos 2\psi + U \sin 2\psi) \tag{1}$$
$$V_{xy} = g_x^i g_y^k [(d_x^i - d_y^{k\,*})I - Q\sin 2\psi + U\cos 2\psi + jV] \tag{2}$$
$$V_{yx} = g_y^i g_x^k [(d_x^{k\,*} - d_y^i)I - Q\sin 2\psi + U\cos 2\psi - jV] \tag{3}$$
$$V_{yy} = g_y^i g_y^k (I - Q\cos 2\psi - U \sin 2\psi) \tag{4}$$

Any polarized signal from the source is present in all four correlations and varies with parallactic angle $\psi$. Consequently, the source polarization signal will effects both the gain solutions and the leakage. The accuracy of the Stokes $Q$ response ($V_{xx} - V_{yy}$ is dependent on the knowledge of the complex gains $g_x$ and $g_y$. Precise measurement of the gains and the leakage terms can be achieved using a strong unpolarized source for which the equations reduce to

$$V_{xx} = g_x^i g_x^k I \tag{5}$$
$$V_{xy} = g_x^i g_y^k (d_x^i - d_y^{k\,*})I \tag{6}$$
$$V_{yx} = g_y^i g_x^k (d_x^{k\,*} - d_y^i)I \tag{7}$$
$$V_{yy} = g_y^i g_y^k I \tag{8}$$

These equations cleanly separate the gain solution into the parallel-hand correlations and the leakage into the cross-hand correlations. As a first step in the calibration we use the observations of J1939-6342 to measure the frequency-dependent $g_x$ and $g_y$ gains. We then apply the gain solutions and derive the leakage terms also using J1939-6342.

All of the target sources are strong compact objects at the phase and pointing centre of the observation. We derive gain solutions for each source by running `gaincal` on each source (essentially a self-calibration assuming a point source model). The absolute $g_x$ and $g_y$ and leakage solutions from J1939-6342 are applied to each source before `gaincal`. We use `gaintype = T`, which average the $xx$ and $yy$ data before solving for the gain. The local gain solution for each source therefore does not modify the relative $g_x$ and $g_y$ gains derived from the bandpass calibrator thus preserving the polarization calibration, and the gain solution is not affected by any polarisation of the source, as can be seen from inspection of equations 1 and 4.

$$V_{xx} + V_{yy} = (g_x^i g_x^k + g_y^i g_y^k) I \tag{9}$$

The gain solution for each sources is thus a local, polarization-independent correction to the absolute gain solution from J1939-6342.

The target sources are distributed over the sky. The transfer of the absolute gain solution from J1939-6342 thus occurs across a large angle on the sky. At GHz frequencies the gain of the system is largely determined by the instrument. The atmosphere plays a minor role. This approach to calibration is thus practical for frequencies in the GHz regime. At higher frequencies where the atmosphere has a strong impact on the gains, or at lower frequencies where the ionosphere will strongly affect the $x - y$ phase, this approach may not be practical.

The last step of the calibration is to solve for any remaining $x-y$ phase using the scan on the polarization calibrator J1331+3030 (3C286). The absolute gain solutions solutions and leakage from J1939-6342 is applied in advance, so this is a residual correction to the solution from the unpolarised primary.

As a check on the $x - y$ phase post calibration we examined the calibrated Stokes spectrum of J1331+3030. A residual error in $x - y$ phase has the effect of rotating flux between $U$ and $V$. For a linear polarized source known to have no circular polarisation $V = 0$, the $x - y$ phase residual can be measured as

$$\Delta\phi_{xy} = \arctan\left(\frac{V}{U}\right) \tag{10}$$

The residual $x - y$ phase on 3C 286 after calibration as a function of frequency for each observing run is shown in Figure 1. The residual phase is small, with a maximum of about $2^\circ$ at the low end of the band and close to zero at the high end. An $x - y$ phase error of $2^\circ$ results in a rotation of 0.06% between $U$ and $V$. While small, under the assumption that the Stokes $V$ flux of 3C 286 is actually zero, this final residual $x - y$ phase can in principle be corrected for post-calibration.

The calibration process does not intrinsically solve for the absolute polarization angle of the instrument gain. We derive this post-calibration from the spectra of 3C 286. The observed frequency dependence of the polarisation angle for 3C 296 for each observing run is shown in Figure 2. Assuming a source position angle of $33^\circ$ that is constant with frequency, the position angle correction is shown by the green dots. The green line, which is a polynomial fit to the correction and is applied to all source spectra after imaging. The position angle correction is similar but not identical between runs. The correction on the second run is a few degrees larger than the first. This level of difference could be explained by different ionospheric conditions. Scaling the measurement of ionospheric Faraday effects by Ericson et al. [2] at 333 MHz to 1400 MHz as $\lambda^2$, the expected variations in polarization position angle from the ionosphere at L-band is of order a few degrees.

Following calibration a full Stokes cube for each sources was created using the IDIA cube generation pipeline component[2] written by Lennart Heino. The cubes contain Stokes $I$, $Q$, $U$, $V$ images versus frequency in 320 channels, each of width 2.51 MHz. Each channel image is $512 \times 512$ pixels with pixel cell size of $1.5''$. Full Stokes spectra

[2] `https://github.com/idia-astro/mightee-pol`

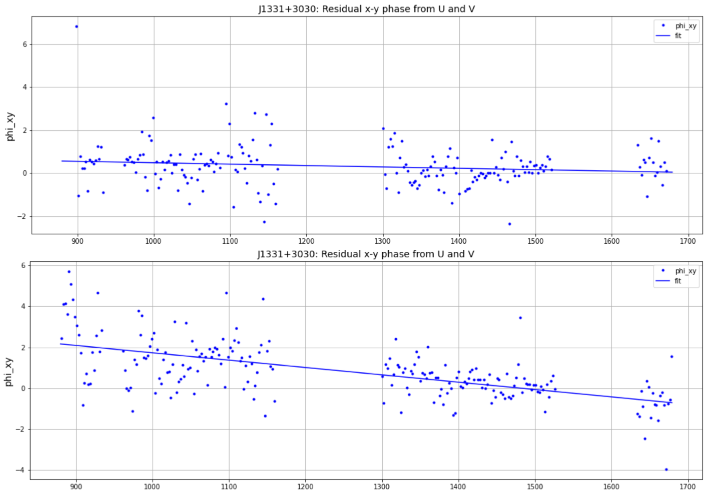


Figure 1: The residual $x - y$ phase angle (degrees) measured from the Stokes $U$ and $V$ spectra of J1331+3030 (3C 286). The top panel shows $\phi_{xy}$ versus frequency for the first run and the bottom for the second run. The line is a linear fit.

for each source were constructed by extracting the peak flux in the $I$, $Q$, $U$ and $V$ at the location of the peak Stokes $I$ flux density in each channel.

# 4 Results

Table 3 at the end of this document list the following properties for each calibration source.

1. the flux density at 1400 MHz ($S_{1.4}$), from a power-law fit the to Stokes I spectrum.
2. the in-band spectral index from the power-law fit to the Stokes $I$ spectrum ($\alpha$). Errors is the formal error on the fit parameter from the covariance matrix.
3. the percent polarized intensity and position angle at 1400 MHz ($p_{1.4}$, $pa_{1.4}$) measured as the average value of polarised intensity and polarization angle over the channels within $\pm$20 MHz of 1400 MHz. The errors are the standard error on the mean derived from the RMS of the $N$ values over the frequency interval divided by $\sqrt{N}$.
4. the spectral index of polarized intensity ($\beta$) from a power-law fit to the spectrum of polarized intensity. Errors are the formal error on the fit parameter from the covariance matrix.
5. the Faraday depth of the dominant RM synthesis component with error.
6. the amplitude (polarized intensity) of the dominant RM synthesis component.

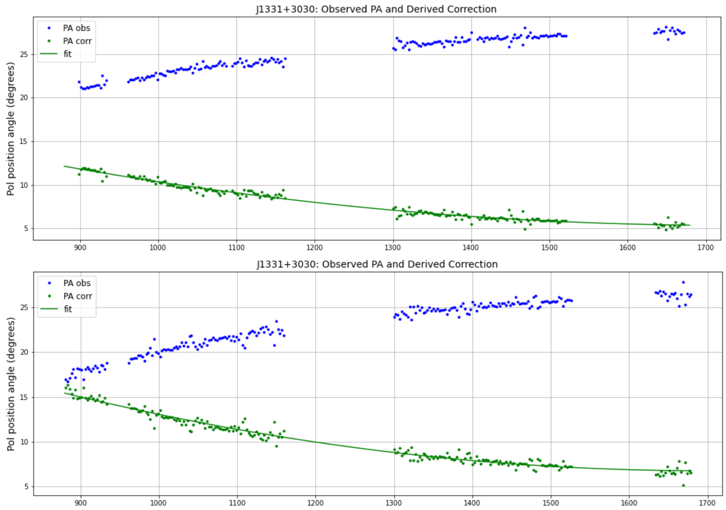


Figure 2: The observed polarization position angle versus frequency for J1331+3030 (blue dots), and the derived position angle correction (green). The top panel shows the result for the first observing run and the bottom for the second run. The green line is a polynomial fit to the position angle correction that is applied to all sources.

7. the median value fractional Stokes v=V/I over the band. The error is the standard error on the mean derived from the RMS of the values over the band.

The errors listed for $p_{1.4}$ and v include only the random error from the variance of the data over the spectral interval used to derive the mean and median. The spectral variance is much smaller than the residual instrumental leakage error, which is estimated as 0.16% in p and 0.06% in v. Detection thresholds have been taken as 0.2% for p and 0.1% for v.

Plots of the Faraday synthesis spectra, frequency spectra of total intensity, and Stokes Q and U versus $\lambda^2$ for each source are available on Ilifu in the directory: /idia/projects/meerkat-cal/spectral_plots/, with file names <sourcename>RMspec.png, <sourcename>I.png and <sourcename>QUlamda.png.

## 4.1 Total Intensity Properties

Figure 3 shows the distribution of in-band spectral indices for the sources. The median spectral index is $-0.39$. This is flatter than typical of the general source population, which is more typically $-0.7$. This difference can be attributed to the fact that the calibrator sources are selected for brightness and compactness. The optical depth to synchrotron self-absorption is proportional to $(S^{\frac{2}{5}}\theta^{-\frac{4}{5}})$, where $\theta$ is the angular dimension of the source, so synchrotron self-absorption will be more dominant than in the general population.

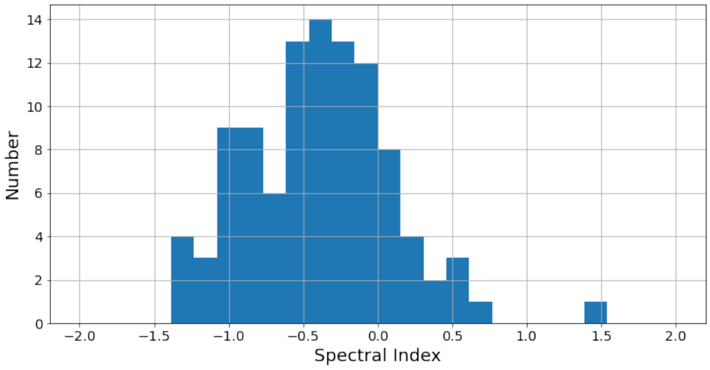


Figure 3: The distribution of in-band spectral indices.

Figure 4 compares the flux density at 1400 MHz from MeerKAT and NVSS. The dashed line is not a fit. It shows the 1:1 relation. There is a core of sources that fall on the 1:1 line. These sources are apparently flux stable on time scales of 20 years. Two strong sources exhibit high fractional variability, J1924-2914 decreased from 13.4 Jy to 4.9 Jy since the mid 1990's when the NVSS observation were made. J2253+1608 increased from 12.7 Jy to 16.2 Jy. Several of the fainter sources also show variability. Again, given the compactness criteria for the source selection, the presence of significant variability, particularly over time scales of decades, is to be expected.

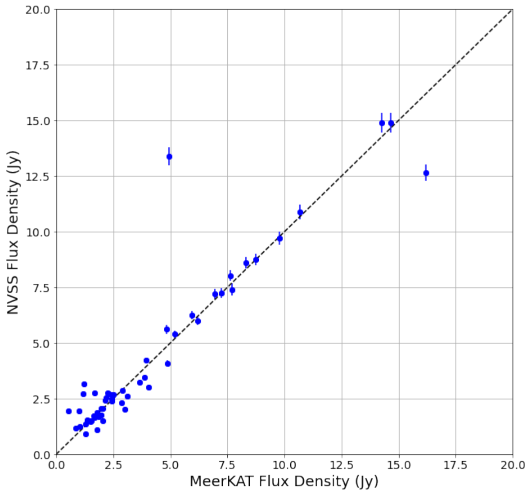


Figure 4: Comparison of the Flux density at 1400 MHz from MeerKAT and NVSS. The dashed line shows the 1:1 relation.

### 4.2 Polarization Properties of the Calibrators

The band-averaged fractional linear polarization of the calibrator sources was measured by taking the median of the per channel polarized intensity $p_{\mathrm{med}}$. The per channel polarized intensity is just the per-channel ratio of the polarized to total peak intensity.

$$p_i = \frac{\sqrt{Q_i^2 + U_i^2}}{I_i}, \tag{11}$$

where $i$ is the channel number. $p_{\mathrm{med}}$ is the median of the $p_i$ values. The band-centre frequency is 1278.0 MHz. For comparison to other published results, e.g. the NVSS, we also calculated the polarized intensity at 1400 MHz as the average polarized intensity over the all channels within ±20 MHz of 1400 MHz. A third measure of the polarized intensity is the value of the peak of the dominant component in the Faraday Synthesis spectrum. This is an equivalent measure of the median intensity only in the case that there is a single Faraday component. In practice multiple Faraday components of Faraday complexity means the peak Synthesis spectrum peak will underestimate the total polarized intensity of the source. For both $p_{\mathrm{med}}$ and $p_{1.4}$ no correction was made for noise bias, as the effect of noise bias is not significant.

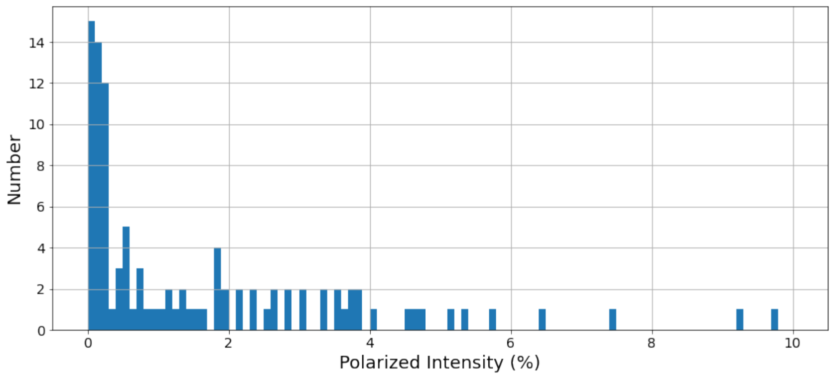


Figure 5: Distribution of fractional polarization $p_{\mathrm{med}}$ for the calibrator sources.

The distribution of polarized intensity $p_{\mathrm{med}}$, for all sources is shown in Figure 5. The distribution is characterized by a broad tail of polarized sources extending up to nearly 10%. There is strong peak near zero that corresponds to sources with no detectable polarization. Assuming that J1939-6342 is unpolarised we can take the observed linear polarization of J1939-6342 as a measure of the residual instrumental polarisation (the level to which the leakage is removed). For the first run on 19 August 2019 the residual polarization on J1939-6342 is 0.164%. For the second run we get a consistent result of 0.160%. Without further analysis we take 0.2% as the minimum detectable polarization. This figure is consistent with the extent of the noise peak in Figure 5.

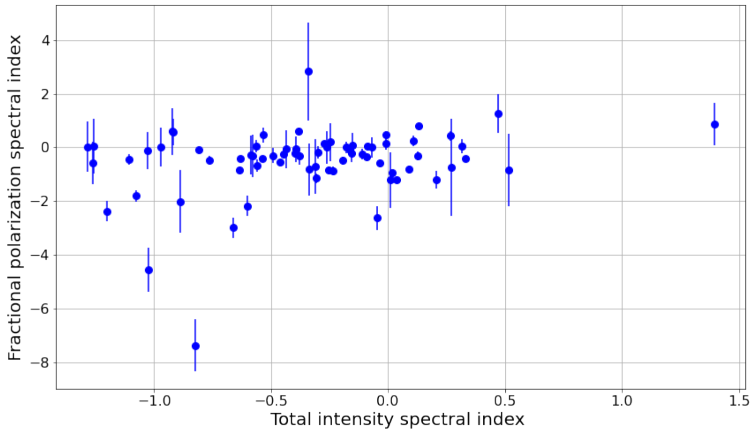


Figure 6: Fractional Polarization spectral index versus total intensity spectral index for 69 source detected in polarization.

We find that 69 of the calibrators sources are detected in polarization above 0.2%. For the polarized sources we calculated the polarization spectral index $\beta$ as

$$p \propto \lambda^{\beta} \tag{12}$$

When $\beta < 0$ a source is classed a "depolarized", i.e. the fractional polarization is smaller at longer wavelengths (lower frequencies). For $\beta > 0$ a source is classed a "repolarized", with fractional polarization increasing toward longer wavelengths. Figure 6 shows a plot of the total intensity spectral index $\alpha$ versus $\beta$. The Figures shows that for flat spectrum sources ($\alpha > -0.5$) the polarized spectral index $\beta$ is typically flat. Strong depolarization is present predominantly for steep spectrum sources. This result confirms a result first report in the study of the polarized SEDs of 951 sources from published polarization measurements by Farnes et al. [3]. The distinction in the polarization properties of steep and flat spectrum sources is taken to demonstrate that depolarization properties of sources are due to local source enivronments.

## 4.3 Potential Wide-band Polarization Calibrators

Several of the sources show fairly strong fractional polarization. There are 30 sources with $p_{\rm med} > 2.0\%$. Many of these have a dominant Faraday Synthesis component at RM of several 10's of rad m$^{-2}$. Calibration sources with high rotation measure complicate polarization calibration over wide-bands at GHz frequencies and below. For the MeerKAT L-band an RM of 10 rad m$^{-2}$ produces a rotation of the polarization angle across the band of 48° and rotates flux between Stokes Q and U over the band. The primary polarization calibrators, 3C 286 and 3C 138, have Rotation Measures very close to zero [7].

| Name | $S_{1.4}$ (Jy) | $p_{1.4}$ (%) | $\mathrm{pa}_{1.4}$ (°) | RM (rad m$^{-2}$) |
|---|---|---|---|---|
| J0059+0006 | 2.45 | 3.76 | 74.3 | -3.6 ± 0.8 |
| J0108+0134 | 3.11 | 3.89 | -79.7 | -6.6 ± 0.5 |
| J1051-2023 | 1.44 | 2.29 | 66.8 | -4.0 ± 1.2 |
| J1239-1023 | 1.55 | 2.50 | 78.8 | 2.4 ± 1.0 |
| J1424-4913 | 8.13 | 1.84 | -4.4 | 10.8 ± 1.5 |
| J1512-0906 | 2.44 | 3.23 | 42.1 | -10.4 ± 0.5 |
| J1517-2422 | 3.03 | 3.35 | 41.1 | -5.4 ± 0.5 |
| J1550+0527 | 2.86 | 1.77 | 77.9 | -6.4 ± 1.6 |
| J1923-2104 | 1.22 | 2.93 | -33.1 | 9.8 ± 0.7 |
| J2131-1207 | 1.97 | 1.75 | -44.1 | 6.8 ± 0.9 |

Table 1: Potential Wide-band polarization calibrators.

Table 1 lists ten objects with fractional polarization greater than 1.5% and the Rotation Measure of the dominant Faraday Synthesis component less than ∼10 rad m$^{-2}$. The table lists the J2000 source name, the total intensity flux density at 1400 MHz, the percent polarization and position angle at 1400 MHz, and the Rotation Measure of the dominant Faraday Synthesis component. Figure 7 shows the amplitude RM synthesis spectra for each. If these objects have stable polarization properties, they would be calibrators for absolute polarization. A monitoring program would allow us to assess their potential for this purpose.

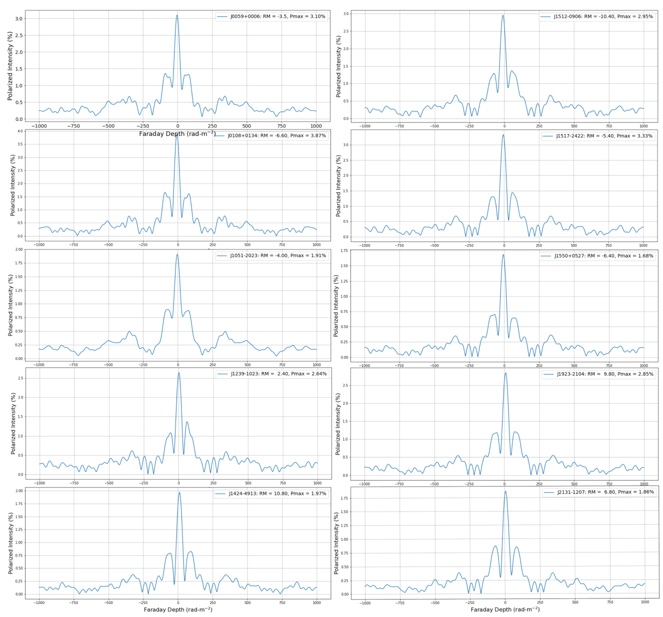

Figure 7: RM synthesis amplitude spectra for the ten sources in Table 1. The spectra are dominated by a single RM component close to zero.

## 4.4 Comparison to NVSS and SPASS

Among the MeerKAT 98 cal sources, 54 are present in the NVSS RM catalog [9] and 20 are found in the SPASS catalogue [6]. Figure 8 shows a comparison of the Faraday depth of the dominant component in the RM synthesis spectra of the MeerKAT calibrators compared to the RM observed with the NVSS at 1.4 GHz and SPASS at 2.3 GHz for sources with percent polarization greater than 1% in the NVSS and SPASS.

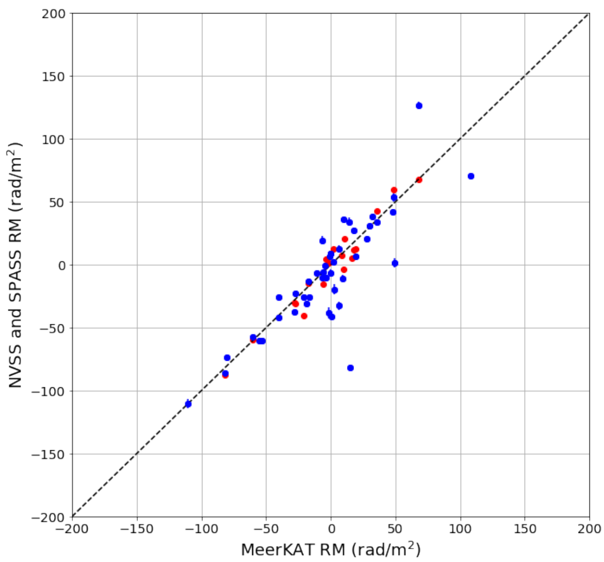


Figure 8: Faraday depth of the dominant RM synthesis component for the MeerKAT calibrators compared to the RM from the NVSS (blue) and SPASS (red).

The SPASS data show very good agreement to the MeerKAT results. As for the MeerKAT data, the SPASS results show the Faraday depth of the dominant component of the RM synthesis spectrum. The NVSS also shows generally good agreement, but with a few outliers. The NVSS observations [1] were taken almost 30 years ago. It is not surprising to see some source vary in RM, particularly given the compact nature of the calibrator source list. We note also that the NVSS RMs were derived from a simple two-point fit to the slope of the position angle with frequency, which will provide a less reliable measure in the presence of Faraday complexity.

The MeerKAT percent polarization at 1400 MHz, $p_{1.4}$, is compared to the NVSS polarization and the SPASS 2.3 GHz polarisation in Figure 9. While there is significant scatter in the data, there is a good correlation. The SPASS polariation tends to be higher on average as expected from depolarisation studies. The average depolarization for ours sample is

$$D = \frac{\pi_{SP}}{\pi_{MK}} = 1.37 \tag{13}$$

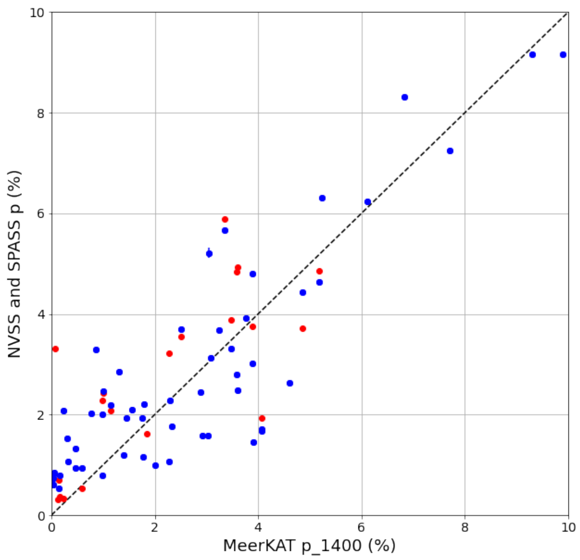


Figure 9: Fractional polarisation (percent) at 1400 MHz for the MeerKAT calibrators compared to the values from the NVSS (blue) at 1400 MHz and from SPASS (red) at 2300 MHz.

which is similar to values found by Lamee et al. [5] between 416 sources detected in both the SPASS and NVSS.

## 4.5 Circular Polarization

The linear feeds of MeerKAT provide the possibility of very precise measurements of circular polarisation, as the circular polarised signals appear only in difference of the the cross-hand correlations (Equations 2 and 3) and is contaminated only by the residual polarization leakage and cross-hand phase errors. Circular polarization of extragalactic sources is notoriously difficult to measure due to the typically very low fractional polarization. We use a strong unpolarized source J1939-6342 to measure the leakage and the frequency-dependence of the $x$ and $y$ phases independently. The absolute cross-hand $(x - y)$ phase difference is calibrated using J1330+2020. After applying the calibration the residual band-averaged Stokes $V$ signal on J1331+3030 is 0.058%. This value is consistent with the residual $x - y$ phase error discussed in section 3. Assuming no circular polarisation for J1331+3030, we can conservatively take this as an estimate of the residual instrumental error on fractional circular polarization.

Figure 10 shows the distribution of fractional Stokes $V$ for the MeerKAT calibrator sources. The distribution is centrally peaked around zero with several outliers. One source, J0240-2309 is very strongly circularly polarized with $V$ close to 0.4%. The standard deviation of the distribution, measured as 1.486 times the median absolute deviation (MAD), is 0.062%.

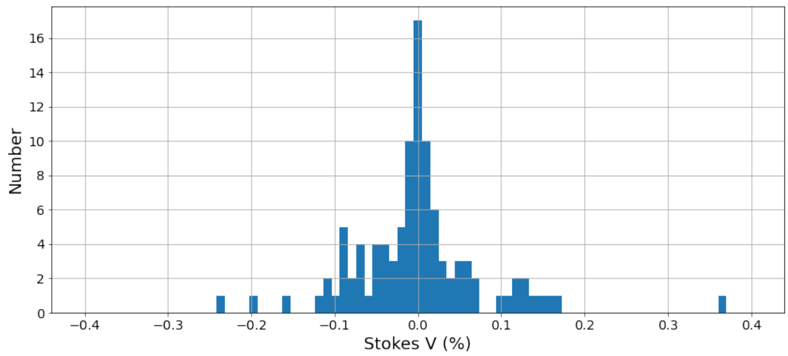


Figure 10: Distribution of band-averaged fractional Stokes $V$ (%) for the MeerKAT calibrator sources.

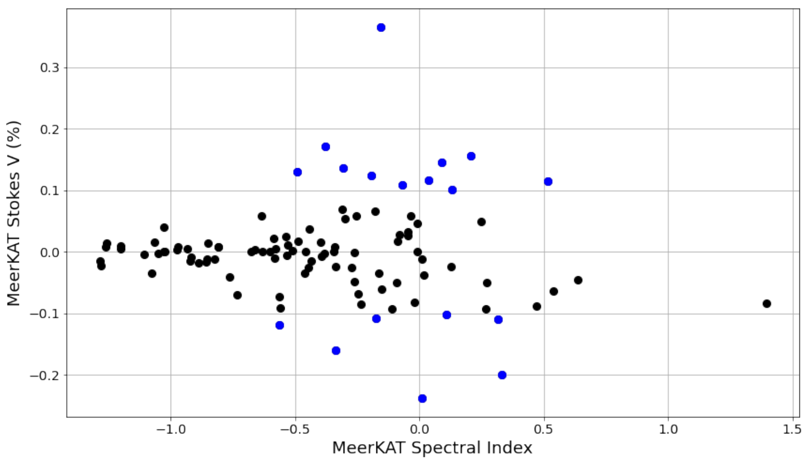


Figure 11: Fractional band-averaged circular polarisation (%) versus the MeerKAT spectral index from the Stokes I spectrum. Sources with measured values of $V > 0.1\%$ are shown in blue.

Figure 11 plots the fractional Stokes $V$ versus the spectral index determined by the fit to the Stokes $I$ spectrum. Source with $V > 0.1\%$ are shown in blue. Circular polarization is detected in 18% of the sources. It is striking that significant circular polarization is detected only for flat spectrum sources with $-0.5 < \alpha < 0.5$ Steep spectrum sources do not exhibit circular polarization. This is consistent with the result of high precision circular polarization measurements of 31 radio sources at 5 GHz with the ATCA [8], which also showed circular polarization only for sources with spectral index $\alpha > -0.5$ between wavelengths of 3 cm−20 cm.

## 5 Limits to the Accuracy of Polarization Calibration

The simple calibration approach described in this document provides a limiting detection level in fractional linear polarization of ∼0.2% and ∼0.1% in fractional circular polarization. This performance is already quite good (particularly in circular polarization) compared to the precision of standard polarization calibration with other interferometer arrays. Nevertheless, the noise level of the data is much lower than these values. The noise levels for each source was determined by measuring the variance of intensity with frequency for an off-source position in each spectral cube. The median noise per channel over all sources in I, Q, U and V is 2.61, 0.30, 0.32 and 0.23 mJy-bm$^{-1}$ respectively. In fractional polarization the median noise in Q/I, U/I and V/I is 0.011, 0.011 and 0.008%. The limits to precision of polarization measurements in our observations is thus not set by the noise, but by residual instrumental polarization after calibration. It is interesting to explore the instrumental effects that give rise to these limits and what might be required to achieve even lower levels of detection.

Figure 12 shows the spectrum of polarized signals for J1939-6342 for the two observing runs. Since the sources is assumed to have zero linear and circular polarization and is used for both the polarization-dependent absolute bandpass calibration and for calibration of the polarization leakage, the polarized signal on this sources represents the residual error of the calibration. The polarization spectra shows signal with structure in frequency and residual levels of about 0.1% in linear polarization - about a factor of 10 higher than the rms noise. The peak-to-peak variation of the signal across the band is similar to the average signal strength. The circularly polarized signal is lower but still present. It should be noted that we have assumed $V = 0$ for J1939-6342. Rayer et. al. [8] have reported a tentative detection of cicular polarization of J1939-6342 at 4.8 GHz of $+0.029 \pm 0.005\%$, so there may be low levels of source signal present in V.

The median and rms values over the band for each Stokes parameter are list in Table 2.

| Date | Q/I | U/I Median (%) | V/I | Q/I | U/I RMS (%) | V/I |
|---|---|---|---|---|---|---|
| 19 August 2019 | 0.082 | 0.142 | 0.026 | 0.033 | 0.039 | 0.016 |
| 29 August 2020 | 0.141 | -0.075 | -0.004 | 0.044 | 0.037 | 0.003 |

Table 2: Band-averaged polarization of J1939-6342 for the two runs.

The residual leakage signals may arise either due to instabilities in the bandpass resulting in time variation in the frequency spectrum of the leakage. It could also arise from variation with pointing direction either due to small changes in the optics with orientation of the antennas or through external direction dependence, e.g. from the ionospheric effects, which can affect both the gain phase and the rotation angle of

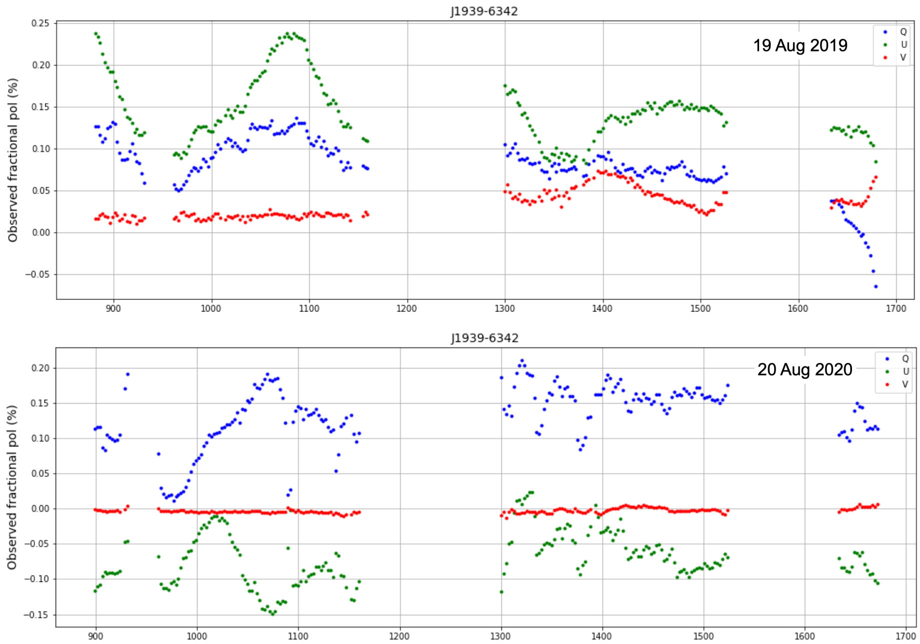


Figure 12: Polarization spectra of J1939-6342 on 19 August 2019 (top) and 29 August 2020 (bottom). For each run, traces are shown for Q/I (blue), U/I (green) and V/I (red).

polarization. As noted in section 2, the ionosphere is expected to introduce a polarization dependent phase variation of order a few degrees at L-band.

During the 19 August 2019 run J1939 was observed five times over a time span of about seven hours. For the 20 August 2020 J1939 was observed three times over a much shorter span of a just under three hours. For the polarization dependent bandpass solution the solution interval was set to 60 minutes to provide a crude time-dependent solution. For the leakage calibration the solint was 'inf', to create a single average leakage solution. Any instabilities or the direction dependence from the average value will propagate through as residual errors.

One may not expect ionospheric effects to result in the frequency structure seen in Figure 12. However, one way to test for the impact of the ionosphere is to carry out an observing run at night time when the ionosphere is not excited by solar radiance. An indication of the impact of night time versus daytime observation is shown in Figure 13. For the second run in August 2020 we observed the strong source J0408-6545 approximately once per hour during the course of the run. The Figure shows the gain amplitude and phase solutions from gaincal as a function of time. These gain solutions were derived after applying the gain solutions from the primary calibrator J1939-6342 and were made with gaintype='T' so the parallel hand correlations are averaged before the solve. If the J1939-6342 solutions were correct for J0408-6545 then the solution gain amplitude solution would be 1.0 and the phase solution would be 0.0. The vertical red line on each plot shows the approximate time of astronomical Sun rise on the date of the observation. It is noteworthy that prior to Sun rise the gains solutions are quite stable and uniformly close to 1.0 in amplitude and 0.0 in phase. The peak-to-peak dispersion is approximately ±0.1% in gain and ±0.3 degrees in phase. About two hours after astronomical Sun rise the dispersion becomes significantly larger, 1-2% in gain and over 1 degree in phase. This strongly suggests that the atmospheric/ionospheric stability is much better during the night (by a factor of several to ten) and thus transfer of gain solutions from the primary calibrator to target sources more precise. This may reduce the level of residual instrumental polarization.

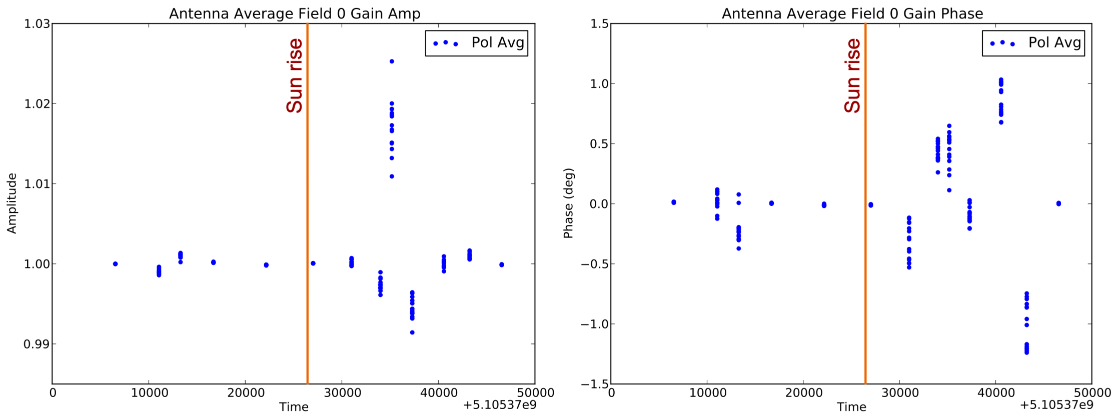


Figure 13: Gaincal solutions for hourly observations of J0408-6545 during the observing run of 29 August 2020. The left hand panel shows gain amplitude versus time and the right hand panel the gain phase versus time. The vertical red line shows the approximate time of astronomical Sun rise.

Table 3: Polarization Properties of MeerKAT Calibrator Sources.

| Name | $S_{1.4}$ (Jy) | $\alpha$ | $p_{1.4}$ (%) | $pa_{1.4}$ (deg) | $\beta$ | RM (rad m$^{-2}$) | $p_{max}$ (%) | v (%) |
|---|---|---|---|---|---|---|---|---|
| J0010-4153 | 4.545 ± 0.102 | -0.851 ± 0.02 | 0.12 ± 0.00 | -60.2 ± 0.7 | -0.240 ± 1.26 | -1.20 ± 18.7 | 0.14 | 0.008 ± 0.002 |
| J0022+0014 | 2.900 ± 0.065 | -0.563 ± 0.02 | 0.09 ± 0.01 | -11.3 ± 1.6 | -1.530 ± 1.66 | 2.00 ± 13.1 | 0.13 | -0.080 ± 0.003 |
| J0024-4202 | 2.871 ± 0.065 | 0.639 ± 0.06 | 0.10 ± 0.01 | -4.1 ± 1.1 | -0.360 ± 1.42 | 4.60 ± 13.2 | 0.13 | -0.052 ± 0.003 |
| J0025-2602 | 8.731 ± 0.196 | -0.733 ± 0.01 | 0.17 ± 0.00 | 72.8 ± 1.1 | 0.310 ± 0.94 | -3.60 ± 12.8 | 0.18 | -0.077 ± 0.004 |
| J0059+0006 | 2.449 ± 0.055 | -0.559 ± 0.01 | 3.76 ± 0.05 | 74.3 ± 0.6 | -0.680 ± 0.23 | -3.60 ± 0.8 | 3.10 | -0.098 ± 0.005 |
| J0108+0134 | 3.113 ± 0.070 | -0.273 ± 0.02 | 3.88 ± 0.01 | -79.7 ± 0.2 | 0.130 ± 0.06 | -6.60 ± 0.5 | 3.87 | -0.033 ± 0.007 |
| J0137+3309 | 16.112 ± 0.362 | -0.889 ± 0.01 | 0.64 ± 0.01 | -36.4 ± 0.5 | -2.010 ± 1.17 | -55.40 ± 4.6 | 0.49 | -0.025 ± 0.003 |
| J0155-4048 | 2.161 ± 0.049 | -0.456 ± 0.01 | 0.07 ± 0.01 | 29.9 ± 2.2 | 1.710 ± 0.90 | 0.00 ± 30.5 | 0.08 | -0.006 ± 0.002 |
| J0203-4349 | 2.726 ± 0.061 | -0.825 ± 0.01 | 0.91 ± 0.01 | -55.5 ± 0.3 | -7.370 ± 0.97 | -8.20 ± 4.8 | 0.49 | -0.018 ± 0.002 |
| J0210-5101 | 3.402 ± 0.077 | 0.127 ± 0.02 | 1.24 ± 0.01 | 30.7 ± 0.2 | -0.310 ± 0.16 | 14.60 ± 2.5 | 1.12 | -0.031 ± 0.003 |
| J0238+1636 | 0.528 ± 0.014 | -0.246 ± 0.05 | 0.77 ± 0.01 | 19.6 ± 23.7 | 0.200 ± 0.71 | 48.00 ± 2.7 | 0.72 | -0.075 ± 0.007 |
| J0240-2309 | 5.938 ± 0.134 | -0.154 ± 0.03 | 0.98 ± 0.00 | -42.2 ± 0.2 | -0.220 ± 0.33 | 10.00 ± 3.0 | 0.98 | 0.359 ± 0.006 |
| J0252-7104 | 5.811 ± 0.131 | -0.972 ± 0.01 | 0.18 ± 0.01 | -35.3 ± 0.2 | 0.010 ± 0.72 | 2.40 ± 12.2 | 0.23 | 0.002 ± 0.001 |
| J0303-6211 | 3.194 ± 0.072 | -0.093 ± 0.01 | 4.71 ± 0.01 | 46.6 ± 0.5 | -0.340 ± 0.07 | 49.60 ± 1.2 | 4.43 | -0.057 ± 0.005 |
| J0318+1628 | 7.619 ± 0.171 | -0.529 ± 0.02 | 0.03 ± 0.01 | -19.9 ± 8.5 | -2.220 ± 2.41 | 5.20 ± 44.2 | 0.05 | 0.004 ± 0.003 |
| J0323+0534 | 2.766 ± 0.062 | -0.920 ± 0.01 | 0.26 ± 0.01 | -71.6 ± 0.3 | 0.590 ± 0.88 | 2.40 ± 8.0 | 0.33 | -0.021 ± 0.003 |
| J0329+2756 | 1.395 ± 0.031 | -0.336 ± 0.02 | 0.16 ± 0.01 | -3.7 ± 1.1 | -0.810 ± 0.97 | 2.40 ± 7.7 | 0.21 | -0.166 ± 0.003 |
| J0403+2600 | 1.289 ± 0.029 | 0.037 ± 0.02 | 3.05 ± 0.01 | 75.3 ± 0.6 | -1.190 ± 0.10 | 49.80 ± 1.3 | 2.62 | 0.110 ± 0.007 |
| J0405-1308 | 3.945 ± 0.089 | -0.533 ± 0.02 | 1.14 ± 0.01 | 31.4 ± 0.3 | 0.460 ± 0.29 | 19.60 ± 2.6 | 1.18 | -0.012 ± 0.002 |
| J0408-6545 | 15.198 ± 0.342 | -1.201 ± 0.00 | 0.01 ± 0.00 | -65.1 ± 0.8 | 1.050 ± 0.69 | 1.20 ± 146.3 | 0.02 | 0.003 ± 0.000 |
| J0409-1757 | 2.205 ± 0.050 | -0.855 ± 0.01 | 0.15 ± 0.01 | -35.3 ± 1.0 | 0.630 ± 0.72 | 5.20 ± 14.0 | 0.20 | -0.018 ± 0.002 |
| J0420-6223 | 3.327 ± 0.075 | -1.050 ± 0.01 | 0.12 ± 0.01 | 65.7 ± 0.4 | 0.000 ± 0.71 | 2.60 ± 14.8 | 0.16 | -0.009 ± 0.001 |
| J0423-0120 | 1.195 ± 0.027 | -0.088 ± 0.04 | 4.07 ± 0.01 | 39.0 ± 0.2 | 0.060 ± 0.10 | -20.60 ± 1.2 | 3.98 | 0.011 ± 0.007 |
| J0440-4333 | 3.593 ± 0.081 | -0.763 ± 0.01 | 0.60 ± 0.01 | -76.6 ± 0.2 | -0.480 ± 0.16 | 8.40 ± 3.8 | 0.57 | -0.047 ± 0.001 |
| J0447-2203 | 2.025 ± 0.046 | -1.029 ± 0.01 | 0.23 ± 0.01 | -24.6 ± 0.5 | -0.130 ± 0.69 | 2.00 ± 8.6 | 0.28 | -0.007 ± 0.003 |
| J0453-2807 | 2.193 ± 0.049 | -0.342 ± 0.01 | 0.59 ± 0.04 | 17.0 ± 1.5 | 2.830 ± 1.82 | 19.60 ± 2.0 | 1.73 | 0.002 ± 0.004 |
| J0503+0203 | 2.218 ± 0.050 | 0.249 ± 0.03 | 0.04 ± 0.00 | 41.6 ± 1.7 | 1.520 ± 0.98 | 1.60 ± 46.8 | 0.06 | 0.042 ± 0.003 |
| J0521+1638 | 8.332 ± 0.187 | -0.636 ± 0.01 | 7.71 ± 0.05 | -8.2 ± 0.2 | -0.830 ± 0.05 | -0.80 ± 0.3 | 7.03 | 0.052 ± 0.007 |
| J0534+1927 | 6.741 ± 0.152 | -0.856 ± 0.01 | 0.02 ± 0.01 | -4.0 ± 10.7 | -2.060 ± 2.04 | 6.40 ± 48.5 | 0.05 | -0.023 ± 0.002 |
| J0538-4405 | 2.156 ± 0.049 | -0.336 ± 0.03 | 0.07 ± 0.00 | 70.8 ± 1.0 | 3.250 ± 0.99 | 48.80 ± 17.7 | 0.17 | -0.030 ± 0.001 |
| J0609-1542 | 1.674 ± 0.038 | -0.562 ± 0.04 | 2.28 ± 0.01 | 9.2 ± 0.9 | 0.050 ± 0.23 | 68.40 ± 1.3 | 2.45 | -0.126 ± 0.004 |

Continued on next page

Table 3 – continued from previous page

| Name | $S_{1.4}$ (Jy) | $\alpha$ | $p_{1.4}$ (%) | $pa_{1.4}$ (deg) | $\beta$ | RM (rad $m^{-2}$) | $p_{max}$ (%) | v (%) |
|---|---|---|---|---|---|---|---|---|
| J0616-3456 | 2.904 ± 0.065 | -0.583 ± 0.01 | 0.13 ± 0.01 | -54.1 ± 17.3 | 0.220 ± 0.62 | 1.40 ± 10.3 | 0.16 | -0.017 ± 0.001 |
| J0632+1022 | 2.427 ± 0.055 | -0.435 ± 0.03 | 0.24 ± 0.01 | 37.0 ± 0.9 | -0.060 ± 0.70 | 2.60 ± 10.3 | 0.27 | -0.021 ± 0.002 |
| J0725-0054 | 11.733 ± 0.264 | 0.333 ± 0.03 | 2.52 ± 0.01 | -13.2 ± 0.6 | -0.430 ± 0.10 | 48.80 ± 1.4 | 2.39 | -0.206 ± 0.004 |
| J0730-1141 | 2.260 ± 0.051 | 0.473 ± 0.04 | 0.98 ± 0.01 | -72.9 ± 1.7 | 1.270 ± 0.73 | 108.00 ± 1.7 | 1.49 | -0.095 ± 0.002 |
| J0735-1735 | 2.600 ± 0.059 | -0.173 ± 0.01 | 0.06 ± 0.00 | 50.0 ± 2.2 | -1.410 ± 1.39 | 0.00 ± 38.9 | 0.07 | -0.115 ± 0.002 |
| J0739+0137 | 1.021 ± 0.023 | 0.133 ± 0.03 | 5.24 ± 0.02 | -81.9 ± 0.4 | 0.790 ± 0.06 | 27.60 ± 1.3 | 5.81 | 0.094 ± 0.006 |
| J0745+1011 | 3.225 ± 0.073 | 0.518 ± 0.04 | 0.22 ± 0.01 | 46.4 ± 0.4 | -0.840 ± 1.34 | 3.20 ± 9.9 | 0.27 | 0.109 ± 0.003 |
| J0825-5010 | 6.244 ± 0.141 | 0.541 ± 0.05 | 0.23 ± 0.01 | 61.3 ± 2.2 | 1.300 ± 1.32 | 1.40 ± 15.3 | 0.12 | -0.071 ± 0.002 |
| J0828-3731 | 2.087 ± 0.047 | -0.261 ± 0.02 | 0.35 ± 0.01 | -83.9 ± 0.2 | 0.010 ± 0.61 | 1.60 ± 4.0 | 0.45 | -0.055 ± 0.001 |
| J0842+1835 | 1.039 ± 0.024 | -0.305 ± 0.02 | 3.09 ± 0.03 | 13.9 ± 0.3 | -1.150 ± 0.19 | 32.20 ± 1.2 | 2.60 | 0.129 ± 0.005 |
| J0854+2006 | 2.047 ± 0.046 | 0.090 ± 0.01 | 6.83 ± 0.02 | 29.8 ± 0.3 | -0.820 ± 0.09 | 29.80 ± 1.0 | 6.05 | 0.139 ± 0.008 |
| J0906-6829 | 1.818 ± 0.041 | -1.107 ± 0.01 | 2.27 ± 0.01 | -27.0 ± 0.5 | -0.440 ± 0.20 | -48.00 ± 1.4 | 2.06 | -0.011 ± 0.002 |
| J1008+0730 | 6.533 ± 0.147 | -0.919 ± 0.01 | 0.22 ± 0.01 | -5.9 ± 0.2 | 0.560 ± 0.49 | 0.20 ± 6.0 | 0.30 | -0.016 ± 0.002 |
| J1051-2023 | 1.442 ± 0.032 | -1.075 ± 0.01 | 2.30 ± 0.01 | 66.7 ± 0.1 | -1.800 ± 0.21 | -4.00 ± 1.2 | 1.91 | -0.041 ± 0.003 |
| J1058+0133 | 3.672 ± 0.083 | -0.255 ± 0.01 | 4.07 ± 0.01 | -11.5 ± 0.5 | -0.830 ± 0.11 | -39.80 ± 1.2 | 3.65 | 0.052 ± 0.005 |
| J1120-2508 | 1.638 ± 0.020 | -0.599 ± 0.02 | 1.46 ± 0.00 | -32.1 ± 0.2 | -2.180 ± 0.37 | 9.00 ± 1.5 | 1.14 | -0.007 ± 0.002 |
| J1130-1449 | 4.838 ± 0.059 | -0.234 ± 0.02 | 4.85 ± 0.01 | 71.2 ± 0.5 | -0.870 ± 0.15 | 36.20 ± 1.0 | 4.27 | -0.092 ± 0.004 |
| J1154-3505 | 6.084 ± 0.074 | -0.510 ± 0.02 | 0.16 ± 0.01 | 49.1 ± 1.1 | 1.700 ± 1.17 | -4.80 ± 8.8 | 0.19 | -0.005 ± 0.001 |
| J1215-1731 | 1.700 ± 0.021 | -0.397 ± 0.03 | 2.01 ± 0.00 | 11.9 ± 0.2 | -0.220 ± 0.15 | -14.60 ± 1.5 | 1.88 | 0.009 ± 0.002 |
| J1239-1023 | 1.554 ± 0.019 | -0.068 ± 0.03 | 2.51 ± 0.01 | 78.8 ± 0.2 | -0.000 ± 0.38 | 2.40 ± 1.1 | 2.64 | 0.102 ± 0.003 |
| J1246-2547 | 0.854 ± 0.013 | -0.009 ± 0.06 | 3.48 ± 0.01 | -25.4 ± 0.3 | 0.480 ± 0.11 | -28.20 ± 1.1 | 3.67 | 0.040 ± 0.004 |
| J1256-0547 | 9.782 ± 0.120 | -0.490 ± 0.05 | 3.61 ± 0.01 | -39.8 ± 0.3 | -0.300 ± 0.27 | 17.80 ± 0.9 | 3.43 | 0.124 ± 0.002 |
| J1311-2216 | 4.857 ± 0.060 | -1.281 ± 0.04 | 0.05 ± 0.00 | 18.5 ± 7.1 | -0.640 ± 2.33 | -12.60 ± 36.9 | 0.04 | -0.029 ± 0.002 |
| J1318-4620 | 2.205 ± 0.027 | -0.934 ± 0.02 | 0.04 ± 0.00 | -18.1 ± 14.8 | 0.170 ± 1.76 | 1.60 ± 30.8 | 0.10 | -0.002 ± 0.002 |
| J1323-4452 | 3.026 ± 0.037 | -0.807 ± 0.03 | 0.11 ± 0.01 | 2.8 ± 2.1 | -0.290 ± 2.14 | 0.80 ± 61.5 | 0.04 | 0.001 ± 0.002 |
| J1331+3030 | 14.259 ± 0.174 | -0.538 ± 0.02 | 9.30 ± 0.02 | 33.1 ± 0.1 | -0.400 ± 0.06 | 0.00 ± 0.2 | 8.90 | 0.018 ± 0.008 |
| J1331+3030 | 14.673 ± 0.330 | -0.630 ± 0.01 | 9.90 ± 0.01 | 33.0 ± 0.1 | -0.420 ± 0.06 | 0.00 ± 0.3 | 9.39 | -0.006 ± 0.007 |
| J1337-1257 | 2.525 ± 0.031 | 0.207 ± 0.04 | 1.01 ± 0.01 | 3.5 ± 0.3 | -1.200 ± 0.33 | -17.20 ± 3.5 | 0.81 | 0.149 ± 0.004 |
| J1347+1217 | 5.213 ± 0.064 | -0.489 ± 0.02 | 0.04 ± 0.00 | 60.0 ± 3.4 | -0.780 ± 1.71 | 8.00 ± 32.8 | 0.04 | 0.011 ± 0.001 |
| J1424-4913 | 8.131 ± 0.099 | -0.382 ± 0.02 | 1.84 ± 0.01 | -4.4 ± 0.2 | 0.610 ± 0.09 | 10.80 ± 1.5 | 1.97 | -0.010 ± 0.001 |
| J1427-4206 | 4.464 ± 0.055 | -0.045 ± 0.02 | 2.00 ± 0.01 | -46.1 ± 0.4 | -2.620 ± 0.44 | -39.60 ± 1.4 | 1.54 | 0.026 ± 0.002 |
| J1445+0958 | 2.166 ± 0.027 | -0.378 ± 0.03 | 0.86 ± 0.00 | -75.7 ± 0.3 | -0.330 ± 0.30 | 14.00 ± 3.1 | 0.78 | 0.165 ± 0.001 |

Continued on next page

Table 3 – continued from previous page

| Name | $S_{1.4}$ (Jy) | $\alpha$ | $p_{1.4}$ (%) | $pa_{1.4}$ (deg) | $\beta$ | RM ($rad\,m^{-2}$) | $p_{max}$ (%) | v (%) |
|---|---|---|---|---|---|---|---|---|
| J1501-3918 | 2.806 ± 0.034 | -0.678 ± 0.02 | 0.19 ± 0.01 | 18.4 ± 0.7 | 0.210 ± 0.65 | 0.80 ± 12.2 | 0.21 | -0.006 ± 0.002 |
| J1512-0906 | 2.442 ± 0.030 | -0.034 ± 0.03 | 3.24 ± 0.01 | 42.0 ± 0.1 | -0.570 ± 0.06 | -10.40 ± 0.7 | 2.95 | 0.051 ± 0.001 |
| J1517-2422 | 3.026 ± 0.037 | -0.009 ± 0.02 | 3.35 ± 0.01 | 41.0 ± 0.2 | 0.130 ± 0.22 | -5.40 ± 0.5 | 3.33 | -0.006 ± 0.003 |
| J1550+0527 | 2.864 ± 0.035 | -0.162 ± 0.02 | 1.77 ± 0.01 | 78.1 ± 0.2 | -0.070 ± 0.10 | -6.40 ± 1.6 | 1.68 | -0.042 ± 0.001 |
| J1605-1734 | 1.376 ± 0.017 | -1.201 ± 0.03 | 2.33 ± 0.02 | -49.1 ± 1.2 | -2.380 ± 0.38 | -110.20 ± 1.5 | 1.93 | -0.002 ± 0.002 |
| J1609+2641 | 4.619 ± 0.057 | -0.310 ± 0.04 | 0.24 ± 0.00 | -47.9 ± 0.7 | -0.710 ± 1.01 | 4.60 ± 7.7 | 0.24 | 0.063 ± 0.002 |
| J1619-8418 | 1.514 ± 0.019 | -1.066 ± 0.03 | 0.04 ± 0.00 | 46.6 ± 14.0 | -0.130 ± 1.25 | 3.20 ± 34.3 | 0.05 | 0.009 ± 0.002 |
| J1726-5529 | 5.208 ± 0.064 | 0.009 ± 0.03 | 0.13 ± 0.00 | -65.5 ± 0.6 | 0.430 ± 0.91 | 0.20 ± 15.3 | 0.18 | -0.019 ± 0.001 |
| J1733-1304 | 6.215 ± 0.076 | -0.299 ± 0.02 | 3.58 ± 0.01 | -79.7 ± 0.8 | -0.180 ± 0.22 | -60.40 ± 1.1 | 3.65 | 0.047 ± 0.002 |
| J1744-5144 | 6.917 ± 0.085 | -0.260 ± 0.02 | 0.10 ± 0.01 | -8.7 ± 1.5 | -1.180 ± 1.48 | -10.00 ± 32.4 | 0.07 | -0.008 ± 0.001 |
| J1830-3602 | 7.227 ± 0.088 | -1.286 ± 0.02 | 0.30 ± 0.01 | -80.4 ± 0.6 | 0.020 ± 0.93 | 0.40 ± 7.9 | 0.36 | -0.021 ± 0.002 |
| J1833-2103 | 10.665 ± 0.131 | -0.019 ± 0.03 | 0.14 ± 0.01 | -24.9 ± 1.5 | -1.280 ± 1.06 | -8.40 ± 15.6 | 0.11 | -0.089 ± 0.003 |
| J1859-6615 | 1.602 ± 0.020 | -0.976 ± 0.03 | 0.16 ± 0.01 | 9.2 ± 0.8 | -2.350 ± 1.37 | 8.20 ± 32.6 | 0.08 | -0.003 ± 0.002 |
| J1911-2006 | 2.284 ± 0.028 | 0.269 ± 0.02 | 1.79 ± 0.01 | -78.4 ± 1.0 | 0.430 ± 0.18 | -80.40 ± 1.5 | 1.94 | -0.099 ± 0.002 |
| J1923-2104 | 1.215 ± 0.015 | -0.179 ± 0.03 | 2.93 ± 0.01 | -33.1 ± 0.2 | -0.000 ± 0.21 | 9.80 ± 0.8 | 2.85 | 0.060 ± 0.002 |
| J1924-2914 | 4.937 ± 0.061 | -0.447 ± 0.03 | 1.31 ± 0.01 | 3.4 ± 0.2 | -0.260 ± 0.16 | -18.60 ± 2.5 | 1.21 | -0.033 ± 0.002 |
| J1939-6342 | 14.291 ± 0.322 | -0.079 ± 0.05 | 0.15 ± 0.01 | 35.6 ± 0.5 | 0.580 ± 0.58 | 0.60 ± 17.9 | 0.17 | 0.021 ± 0.001 |
| J1939-6342 | 14.554 ± 0.178 | -0.045 ± 0.05 | 0.16 ± 0.01 | -0.2 ± 1.4 | -0.550 ± 0.74 | -1.40 ± 17.4 | 0.15 | 0.019 ± 0.000 |
| J1951-2737 | 1.297 ± 0.016 | -1.022 ± 0.03 | 1.40 ± 0.01 | -80.2 ± 0.4 | -4.540 ± 0.82 | -1.20 ± 2.8 | 0.87 | -0.006 ± 0.003 |
| J2007-1016 | 1.504 ± 0.019 | -0.807 ± 0.02 | 5.18 ± 0.01 | -12.4 ± 0.9 | -0.100 ± 0.07 | -81.60 ± 1.0 | 5.16 | 0.001 ± 0.003 |
| J2011-0644 | 2.628 ± 0.033 | -0.152 ± 0.04 | 0.25 ± 0.01 | -32.0 ± 0.3 | 0.080 ± 0.45 | 1.00 ± 7.4 | 0.25 | -0.068 ± 0.002 |
| J2052-3640 | 1.367 ± 0.017 | -1.258 ± 0.02 | 0.19 ± 0.01 | -79.3 ± 0.7 | 0.040 ± 1.01 | 2.40 ± 10.4 | 0.27 | 0.007 ± 0.002 |
| J2130+0502 | 4.033 ± 0.050 | -0.441 ± 0.03 | 0.07 ± 0.00 | 20.8 ± 1.9 | 0.340 ± 1.40 | 7.00 ± 28.9 | 0.07 | 0.031 ± 0.003 |
| J2131-1207 | 1.970 ± 0.024 | 0.110 ± 0.03 | 1.75 ± 0.01 | -44.1 ± 0.1 | 0.250 ± 0.20 | 6.80 ± 0.9 | 1.86 | -0.109 ± 0.002 |
| J2131-2036 | 1.961 ± 0.024 | -1.027 ± 0.02 | 0.05 ± 0.01 | -3.0 ± 20.3 | -0.930 ± 2.14 | 19.40 ± 49.3 | 0.05 | 0.034 ± 0.003 |
| J2134-0153 | 1.852 ± 0.023 | 0.020 ± 0.03 | 3.91 ± 0.01 | 48.0 ± 0.6 | -0.940 ± 0.12 | 48.80 ± 1.2 | 3.57 | -0.045 ± 0.004 |
| J2136+0041 | 3.867 ± 0.048 | 1.395 ± 0.05 | 0.33 ± 0.02 | -1.6 ± 0.6 | 0.860 ± 0.79 | 0.00 ± 6.7 | 0.44 | -0.090 ± 0.009 |
| J2148+0657 | 3.274 ± 0.040 | 0.011 ± 0.03 | 0.72 ± 0.01 | -12.1 ± 0.4 | -1.210 ± 1.04 | 7.00 ± 3.8 | 0.72 | -0.245 ± 0.003 |
| J2152-2828 | 2.918 ± 0.036 | -0.662 ± 0.03 | 2.89 ± 0.01 | 37.0 ± 0.6 | -2.990 ± 0.39 | -40.40 ± 1.2 | 2.15 | -0.003 ± 0.005 |
| J2158-1501 | 4.053 ± 0.050 | -0.111 ± 0.02 | 4.61 ± 0.01 | -52.8 ± 0.2 | -0.240 ± 0.20 | 14.80 ± 0.5 | 4.45 | -0.099 ± 0.002 |
| J2206-1835 | 6.284 ± 0.077 | -0.343 ± 0.02 | 0.15 ± 0.00 | -42.4 ± 1.2 | 0.520 ± 0.62 | 16.80 ± 11.6 | 0.15 | -0.006 ± 0.002 |
| J2212+0152 | 2.915 ± 0.036 | -0.584 ± 0.03 | 0.49 ± 0.01 | -5.8 ± 0.5 | -0.290 ± 0.73 | 2.00 ± 5.2 | 0.57 | 0.015 ± 0.002 |

Continued on next page

Table 3 – continued from previous page

| Name | $S_{1.4}$ (Jy) | $\alpha$ | $p_{1.4}$ (%) | $pa_{1.4}$ (deg) | $\beta$ | RM ($\mathrm{rad\,m^{-2}}$) | $p_{max}$ (%) | v (%) |
|---|---|---|---|---|---|---|---|---|
| J2214-3835 | 1.810 ± 0.022 | -0.578 ± 0.02 | 0.57 ± 0.01 | -78.8 ± 0.5 | -0.320 ± 0.78 | 2.20 ± 4.6 | 0.62 | -0.001 ± 0.003 |
| J2225-0457 | 7.717 ± 0.094 | -0.461 ± 0.02 | 3.89 ± 0.01 | -60.9 ± 0.3 | -0.530 ± 0.06 | -27.20 ± 1.2 | 3.63 | -0.042 ± 0.002 |
| J2229-3823 | 2.034 ± 0.025 | -1.262 ± 0.02 | 0.46 ± 0.01 | -86.4 ± 0.6 | -0.580 ± 0.80 | 6.40 ± 5.9 | 0.48 | 0.001 ± 0.003 |
| J2232+1143 | 6.939 ± 0.085 | -0.395 ± 0.02 | 3.02 ± 0.01 | -81.7 ± 0.8 | -0.060 ± 0.48 | -53.40 ± 1.3 | 3.41 | -0.014 ± 0.002 |
| J2236+2828 | 1.795 ± 0.023 | 0.272 ± 0.04 | 0.46 ± 0.01 | -39.6 ± 18.5 | -0.740 ± 1.80 | -125.60 ± 2.8 | 0.56 | -0.057 ± 0.003 |
| J2246-1206 | 1.791 ± 0.023 | 0.316 ± 0.04 | 1.56 ± 0.01 | 72.2 ± 0.3 | 0.050 ± 0.26 | -16.40 ± 1.7 | 1.56 | -0.117 ± 0.002 |
| J2253+1608 | 16.199 ± 0.198 | -0.193 ± 0.03 | 6.11 ± 0.02 | 62.8 ± 0.6 | -0.490 ± 0.14 | -55.00 ± 1.0 | 5.60 | 0.118 ± 0.005 |

## References


[1] J. J. Condon, W. D. Cotton, E. W. Greisen, Q. F. Yin, R. A. Perley, G. B. Taylor, and J. J. Broderick. The NRAO VLA Sky Survey. *Astrophysical Journal*, 115:1693–1716, May 1998.

[2] W. C. Erickson, R. A. Perley, C. Flatters, and N. E. Kassim. Ionospheric corrections for VLA observations using Local GPS data. *Astronomy & Astrophysics*, 366:1071–1080, February 2001.

[3] J. S. Farnes, B. M. Gaensler, and E. Carretti. A Broadband Polarization Catalog of Extragalactic Radio Sources. *Astrophysical Journal Supp.*, 212(1):15, May 2014.

[4] Christopher A. Hales. Calibration errors in interferometric radio polarimetry. *The Astronomical Journal*, 154(2):54, jul 2017.

[5] Mehdi Lamee, Lawrence Rudnick, Jamie S. Farnes, Ettore Carretti, B. M. Gaensler, Marijke Haverkorn, and Sergio Poppi. Magnetic Field Disorder and Faraday Effects on the Polarization of Extragalactic Radio Sources. *Astrophysical Journal*, 829(1):5, September 2016.

[6] B. W. Meyers, N. Hurley-Walker, P. J. Hancock, T. M. O. Franzen, E. Carretti, L. Staveley-Smith, B. M. Gaensler, M. Haverkorn, and S. Poppi. A Southern-Sky Total Intensity Source Catalogue at 2.3 GHz from S-Band Polarisation All-Sky Survey Data. *Publ. of the Astr. Soc. of Australia*, 34:e013, March 2017.

[7] R. A. Perley and B. J. Butler. Integrated Polarization Properties of 3C48, 3C138, 3C147, and 3C286. *Astrophysical Journal Supp.*, 206(2):16, June 2013.

[8] D. P. Rayner, R. P. Norris, and R. J. Sault. Radio circular polarization of active galaxies. *MNRAS*, 319(2):484–496, December 2000.

[9] A. R. Taylor, J. M. Stil, and C. Sunstrum. A ROTATION MEASURE IMAGE OF THE SKY. *The Astrophysical Journal*, 702(2):1230–1236, aug 2009.